Exploring the agricultural potential of AgNPs/PlyB221 endolysin bioconjugates as enhanced biocontrol agents

Fernanda Coelho [a,*], Angelica Maria Mazuera Zapata [a], Thales Rafael Machado [a], Fernanda Canduri [b], Valtencir Zucolotto [a]

[a] *Nanomedicine and Nanotoxicology Group, São Carlos Institute of Physics, University of São Paulo (USP), 13566-590, São Carlos, Brazil*
[b] *São Carlos Institute of Chemistry, University of São Paulo (USP), 13566-590, São Carlos, Brazil*

A B S T R A C T

Understanding the formation of corona proteins on AgNPs (silver nanoparticles) is crucial for the development of therapeutic platforms aimed at selectively eliminating super-resistant bacteria. The insights gained from this study can guide the design and optimization of innovative strategies targeting super-resistant bacteria by leveraging the characteristics and behavior of corona proteins on AgNPs. In this study we developed novel nanobioconjugates combining AgNPs and Ply-B221, an endolysin bacteriophage, and investigated the protein corona formation, as well as their activity against *Bacillus cereus*. The results demonstrate that proteins bind to the surface of the AgNPs, evident from a decrease in the surface plasmon resonance (SPR) peak absorption of the AgNPs and a shift in the maximum peak wavelength from 396 nm to 420 nm. Furthermore, DLS measurements reveal an increase in the hydrodynamic diameter of AgNPs from 4 nm to a plateau of approximately 2000 nm, accompanied by a change in zeta potential from -30 mV to -15 mV. These findings suggest that AgNPs are encased by proteins through electrostatic interactions. The AgNPs/PlyB221 complex effectively reduced the turbidity of *Bacillus cereus* by 80 %, at a concentration of 8.125 x 10^{-6} M. The implications of these findings are significant for the development of theranostic platforms for agricultural use. They provide valuable insights into designing effective strategies to combat super-resistant bacteria using corona proteins on AgNPs.

1. Introduction

The extensive use of antibiotics in agriculture has adversely affected the microbiota of agricultural soils (Mann et al., 2021) contributing to the clinical challenge of antibiotic-resistant diseases in human medicine (Chang et al., 2014). The current century has witnessed the emergence of a plethora of microorganisms that have swiftly and efficiently modified their genes, rendering them resistant to various antibiotic groups (Mann et al., 2021). The proliferation of these pathogens and the relatively slow development of new drugs have constrained new treatment and prevention strategies (Hu et al., 2020). Consequently, the detection of these pathogenic bacteria has become a pivotal area of interest in the realms of food and water safety, public health, and bioterrorism (Tolba et al., 2012).

Bacillus cereus, a widely disseminated gram-positive spore-forming bacterium in the natural environment (Kong et al., 2019), has attracted attention due to its ability to produce various toxins, including enterotoxins, phospholipases, hemolysins, and an emetic toxin (cereulide). These toxins have been frequently linked to severe local and systemic infections, as well as cases of food

poisoning (Bottone, 2010). Concerns have arisen in the food industry regarding psychrotolerant isolates of *B. cereus* due to their potential for growth at low temperatures, toxin production, cross-protection phenomena with other environmental stresses, and implications in foodborne outbreaks (Park et al., 2020). Although most *B. cereus* isolates are susceptible to commonly used antibiotic agents, prolonged and extensive antibiotic use has given rise to multidrug-resistant bacteria. Certain *B. cereus* isolates from food sources have been reported as resistant to beta-lactam antibiotics, tetracycline, erythromycin, rifampicin, vancomycin, aminoglycosides, and fluoroquinolones (Kong et al., 2019).

In recent years, nanomedicine has emerged as a strategic area of study with innovative applications in therapy and diagnostics (Kulshrestha and Khan, 2018). Numerous applications of nanomaterials for diagnosis and treatment have been described in the literature (Caruso et al., 2012; Miller et al., 2015). Nanomaterials hold the potential to overcome some of the key challenges in the clinical world, notably antimicrobial resistance (Kulshrestha and Khan, 2018). Among the nanomaterials, silver nanoparticles exhibit a broad spectrum of antimicrobial activity (Lara et al., 2010). The Ag + ions present on the surface of nanomaterials interact with thiol groups in bacterial cell walls, creating pores in the membrane and inducing cell death (Hajipour et al., 2012).

Bacteriophage endolysins are antimicrobial proteins capable of degrading bacterial peptidoglycan (PG), resulting in bacterial death through cell lysis (Chang, 2020). Combining cationic nanoparticles with endolysins has been shown to enhance the antibacterial activity of the complex (Ciepluch et al., 2019). Moreover, bacteriophage endolysins are gaining prominence as biomaterials for therapeutic applications due to their antimicrobial efficiency and promising economic potential (Caruso et al., 2012). Endolysin PlyB221 exhibits strong affinity and specificity for recognizing the pathogenic bacteria, *B. cereus* (Leprince et al., 2020).

The adsorption of biomolecules to the surroundings of nanoparticles can modulate the surface characteristics of NPs (Cao et al., 2019). This interaction results in the formation of a surface layer of proteins known as the corona protein (Ciobanu et al., 2022; Dawson and Yan, 2021; Paino and Zucolotto, 2015). The affinity of proteins for the nanoparticle surface is influenced by factors such as size, chemistry, and surface potential. Corona protein formation occurs in two distinct modes: hard corona and soft corona, with hard corona having higher dissociation constants compared to the soft corona (Chang et al., 2014). Additionally, the wettability properties of nanoparticles can influence the association and dissociation rates of corona proteins, thereby affecting their relative affinity (Ciobanu et al., 2022; Dawson and Yan, 2021).

In this article, we employ qualitative and quantitative techniques to characterize AgNPs and the PlyB221-AgNPs complex, which holds significant applications in agriculture. Thermal, microscopic and spectroscopic analyses are employed to investigate the size distribution, morphology, and interactions within the complex. Experimental investigations into lytic activity demonstrated that the complex of AgNPs with PlyB221 exhibited enhanced effectiveness against *B. cereus* when compared to the individual constituents.

2. Material and methods

2.1. Nanocomplexes preparation

2.1.1. AgNPs

AgNPs were produced through a modified chemical reduction method. (Jana et al., 2001). The reaction involved the reduction of silver nitrate (AgNO$_3$, 99 %, Sigma-Aldrich) by sodium borohydride (NaBH$_4$, 99 %, Sigma-Aldrich) as the reducing agent, along with the presence of sodium citrate (99 %, Sigma-Aldrich) to enhance AgNPs stability. The synthesis was carried out in an ice bath (4 °C) with low light exposure for 30 min. During this time, 10 mL of NaBH$_4$ (27 mM) and 45 mL of sodium citrate (0.67 mM) were mixed. Subsequently, 45 mL of AgNO$_3$ (0.67 mM) was added drop by drop to the system. After completion, the system was maintained under the same conditions for 2 h. The resulting suspension was then centrifuged at 12,000 × g for 30 min, and the pellet was resuspended in sodium citrate (0.3 mM). The AgNPs suspension was stored at 4 °C, protected from light.

2.1.2. PlyB221 endolysin

The methodology for PlyB221 endolysin expression and purification was based on literature (Leprince et al., 2020). The protein concentration was adjusted between 10 μg/ml - 1 mg/ml for the interaction tests with AgNPs and protein corona formation.

2.1.3. PlyB221- AgNPs complex - protein corona

The silver nanoparticles (2,6. 10^{-6} M) were incubated in solutions containing different concentration of PlyB221 (10μg/ml - 1 mg/ml). The complexes were incubated at room temperature for 1 h, centrifuged, and subsequently characterized.

2.2. Materials characterization

The characterization of AgNPs involved UV–Visible spectrometry (UV–Vis), Fourier Transform Infrared Spectroscopy (FTIR), Dynamic Light Scattering (DLS), Scanning Electron Microscopy (SEM), and Transmission Electron Microscopy (TEM) The protein corona was characterized using UV–Vis, titration-dynamic light scattering (DLS), FTIR, TEM, and Isothermal Titration Calorimetry (ITC).

The formation of silver nanoparticles was confirmed by UV–Vis spectroscopy (Hitache U2900). UV–Vis spectra was obtained using a 1:10 dilution of deionized water using a quartz cuvette. PlyB221 at varying concentrations (0.1 mg/ml - 0.4 mg/ml) was incubated with AgNPs (2.6 × 10^{-6} M) at room temperature for 1 h, and the emission spectra were recorded from 200 to 600 nm.

FTIR spectra of the AgNPs, PlyB221 protein, and protein-nanoparticle complexes were obtained using a FTIR spectrophotometer (Nicolet 6700/GRAMS Suite). The samples were dripped (10 μL) onto a silicon wafer (Si/SiO$_2$/B) and a dry film was obtained by evaporation of the solvents under vacuum. Measurements were performed at room temperature, immediately after drying the samples. The spectra were recorded at 64 scans, with a resolution of 4.0 cm-1 by transmission, in the wavenumber range 500–4000 cm^{-1}.

Through dynamic light scattering (DLS), nanoparticle size distribution and zeta potential were evaluated using Zetasizer Nano ZS90 (Malvern Instruments). The nanoparticles were diluted in a 1:10 ratio with deionized water, and three independent measurements were conducted. Protein formation was evaluated by titration of PlyB221 protein (1 mg/ml) in AgNPs (2.6, 10^{-4} mM) using dynamic light scattering (DLS) technique. The measurements were conducted with a Zetasizer Nano-ZS from Malvern Instruments (Worcestershire, United Kingdom), with detection angle of 173°, equipped with an MPT Autotitrator −2 (Multi PurposeTitrator) (Worcestershire, United Kingdom), at 25 °C. Each sample was measured in triplicate, and 7 size and zeta potential determinations for each sample.

The morphology of the silver nanoparticles was evaluated by scanning electron microscopy (SEM). Ten images were collected in different regions using the ZEISS SIGMA VP FEG-SEM. The samples, diluted in ddH2O at 1:10, were deposited in 10 μL on a clean silicon substrate and left to dry at room temperature. Subsequently, the samples were coated with sprayed platinum plasma.

The AgNPs were also evaluated by transmission electron microscopy (TEM) and energy dispersive X-ray spectroscopy (EDS) in a FEI TECNAI G^2F20 microscope operating at 200 kV. Samples were prepared by dropping 3 μL onto carbon film supported copper grids for 60 s and drying with filter paper. The NPs dimensions were estimated by measuring the sizes of 100 NPs in TEM images collected over 10 different regions.

The protein corona was evaluated by TEM with samples at a concentration of 10ug/ml of PlyB221 and 2.6. 10^{-4} mM AgNPs, prepared by the same methodology describe for AgNPs.

Isothermal titration calorimetry (ITC) was employed to measure the enthalpy changes associated with molecular interactions during complex formation. The enthalpy (ΔH) of titration of PlyB221 into the AgNPs solution was estimated using an ITC instrument (Microcalorimeter ITC200, Malvern Instruments Ltd, Worcestershire, UK). Twenty-nine 2 μL aliquots of 0.159 mM PlyB221 suspension were sequentially injected into a 200 μl titration cell initially containing AgNPs solutions. Each injection lasted 4 s, with an interval of 180 s between injections. The solution was stirred at a speed of 750 rpm throughout the experiments, and the temperature in the titration cell was maintained at 25 °C.

2.3. Antibacterial activity

The lytic activity of the endolysin was assessed through a turbidity reduction assay which involves measuring the reduction in OD_{595} caused by enzymatic activity. In brief, an overnight bacterial culture was diluted 100-fold in fresh medium and incubated until it reached mid-log phase (3–4 h). Following centrifugation ($6000 \times g$ for 5 min), the pellet was washed with PBS and resuspended in 50 mM Tris-HCl at pH 8 to achieve an OD595 ranging from 0.6 to 1. From this bacterial suspension, 180 μL was added to each well of a 96-well plate and combined with AgNPs, PlyB221 protein, and protein-nanoparticle complexes at specific concentrations. The plate was incubated at 30 °C in a MultiskanTM FC Microplate spectrophotometer (Thermo Fisher Scientific, Watham, MA, USA), where OD_{595} was monitored every minute for 30 min. Wells containing bacterial suspensions and protein buffer were employed as a control. The dose-response experiment was carried out in *B. cereus* using varying concentrations of endolysin, ranging from 0.253. 10^{-6} M to 8.125. 10^{-6} M, and the results were expressed as inhibition percentages.

Colorimetric activity assays using resazurin were conducted to confirm the antibacterial activity of the nanocomplexes. The assay was performed in a 96-well plate with six different compound dilutions, along with the inclusion of appropriate controls. Each well was inoculated with a concentration of 10^8 CFU/ml of *B. cereus*, briefly cultured overnight, and the plate was incubated at 30 °C for 24 h. After this period, 30 μL of 0.015 % resazurin was added to each well and maintained in the incubator for 4 h. Plate readings were taken using an excitation at 530 nm and emission fluorescence measurement at 590 nm.

The lytic activity was further evaluated using negative-staining electron microscopy. Samples were deposited onto a 400 Cu mesh carbon film TEM grid, and subsequently stained with a 2 % (w/v) uranyl acetate solution. Some uranyl acetate excess was carefully removed using filter paper. Scanning electron microscopy (SEM) images were acquired using a FEI Magellan 400 L FEG-SEM microscope, while transmission electron microscopy (TEM) images were captured with a FEI TECNAI G^2F20 microscope. Both microscopes operated in scanning-transmission electron microscope (STEM) mode.

3. Result and discussion

3.1. PlyB221 endolysin expression and purification

The full PlyB221 gene was successfully cloned into the expression vector pET30a, which was obtained commercially. PlyB221 Endolysin Fig. 1Expression and Purification methods were adapted from Leprince (Leprince et al., 2020).

Fig. 2 shows the purified recombinant proteins demonstrating the expected MW of 39 kDa.

3.2. Characterization of AgNPs and PlyB221- AgNP complex- protein corona

AgNPs were synthesized using silver nitrate ($AgNO_3$) and the reducing agent sodium borohydride ($NaBH_4$), in the presence of sodium citrate, which enhanced the stability of AgNPs. The successful synthesis of AgNPs was visually confirmed by the color change of the solution from colorless to yellow, indicative of nanoparticle formation.

Nanoparticles characterization provides crucial information about their size, shape, distribution and chemical composition, allowing for better control over the synthesis process.

UV–Vis absorption spectroscopy is highly suitable for detecting the wavelength and absorption corresponding to the surface plasmon resonance (SPR) band (Ismail et al., 2019). The electronic spectrum of the freshly prepared solution, with its yellowish color, exhibited a maximum absorption band at approximately 396 nm, as shown in Fig. 3. The presence of AgNPs in the solution was confirmed by the characteristic λ max optical absorption band typical of metallic AgNPs. It is important to note that an increase in parti-
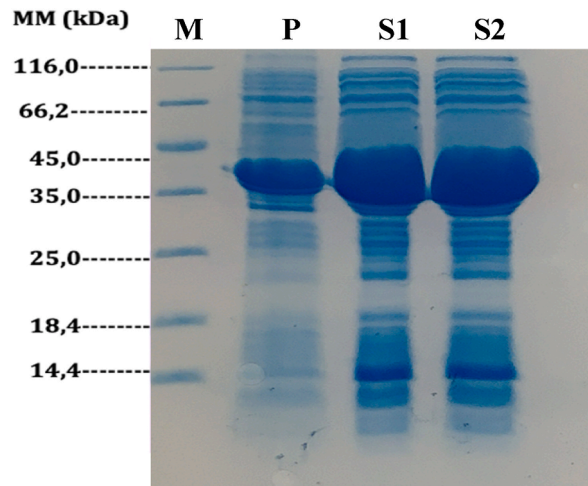
Fig. 1. PlyB221 expression profile in BL21(DE3) cells at 28 °C for 6 h after induction. Samples were subjected to 15 % SDS-PAGE and stained with Coomassie Blue. M: Protein Molecular Weight Marker Thermo Fisher Scientific Inc.); P: resuspended inclusion bodies; S1: soluble fraction of lysed cells and centrifugation to separate insoluble materials; S2: soluble fraction of cells lysed, centrifuged and filtered at 0.45 μm to separate insoluble materials. (For interpretation of the references to color in this figure legend, the reader is referred to the Web version of this article.)
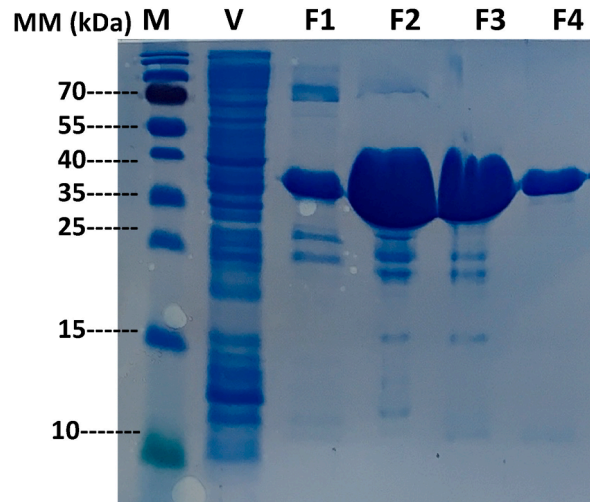
Fig. 2. SDS-PAGE of purified PlyB221 endolysin. M: Protein Molecular Weight Marker (Thermo Fisher Scientific Inc.), V: fraction not bound on the affinity column, F1–F4: fractions washed with 300 mM imidazole.
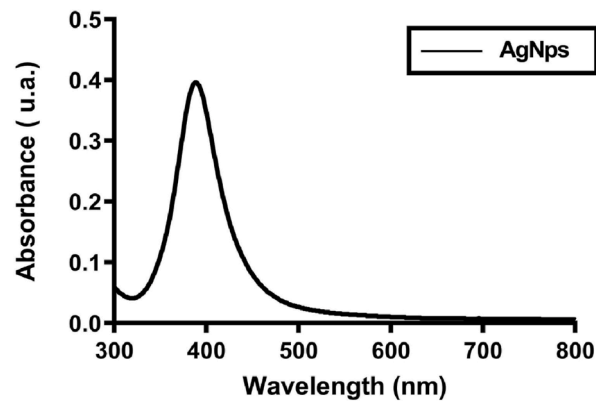

Fig. 3. UV–Vis spectra of the synthesized silver nanoparticles exhibiting a maximum absorption band at approximately 396 nm.

cle size leads to a shift of the absorption band towards longer wavelengths (Pastorizo- Santos and Liz- Marzán, 2009). Additionally, previous studies have established relationships between particle sizes, bandwidth, and solution coloration with the maximum wavelength of absorption bands displayed in electronic spectra (Solomon et al., 2007).

The changes in the Surface Plasmon Resonance (SPR) of AgNPs are well-known sensitive indicators of binding reactions with biomolecules (Banerjee and Das, 2013; Siriwardana et al., 2015). In the UV–Vis spectra, the AgNPs exhibited a characteristic and intense SPR band at 398 nm (Fig. 4 - red line). Upon addition of PlyB221, a decrease in the AgNPs' SPR absorbance was observed, and the wavelength corresponding to the maximum absorbance shifted from 396 nm to 420 nm, indicating the formation of AgNPs-PlyB221 complexes (Fig. 4). The intensity of the SPR absorbance of AgNPs further decreased from 0.40 to 0.22 a.u., suggesting that PlyB221 induced AgNPs dissolution.

The spectroscopic characterization of AgNPs was also carried out via FTIR spectroscopy in the range of 4000 cm^{-1} to 500 cm^{-1} (Fig. 5). A broad band was observed between 3500 and 3300 cm^{-1}, corresponding to OH groups (bending vibration). This band indicated the presence of non-reactive OH groups adhered to the highly reactive surface of the nanoparticles or the absorption of moisture from the surrounding medium during the synthesis process (Aziz et al., 2019; Muzamil et al., 2014). Two bands were observed at 2920 and 2854 cm^{-1} corresponding to C–H stretching vibration. A well-defined band was observed at 1596 cm^{-1}, associated with C=O stretching vibration within the carboxyl group (Aziz et al., 2019; Dara et al., 2020; Muzamil et al., 2014). This higher intensity band is characteristic of silver nanoparticles. Additionally, another prominent band was identified, corresponding to the C–O stretching vibration in the OH$^-$ groups. These various functional groups play a crucial role in the stability of the silver nanoparticles. Although the reduction of silver nitrate was achieved using NaBH4, the presence of sodium citrate ions in the environment of AgNPs also contributed to their stability (Melo et al., 2012). The sodium citrate ions created a non-zero surface charge on the AgNPs, resulting in electrostatic repulsion between the nanoparticles, effectively preventing their aggregation process. This enhanced stability is of great significance in various applications of silver nanoparticles (Dara et al., 2020).

In the spectrum of the PlyB221 protein, the active modes in the infrared region are predominantly represented by the amine bands (Burt et al., 2004; Ghosh and Panicker, 2021; Leprince et al., 2020). The N–H stretching mode appears as a doublet, with amine A bands at 3297 cm^{-1} and amine A′ bands at 3062 cm^{-1}. The amine I band primarily corresponds to the C=O stretching mode, detected
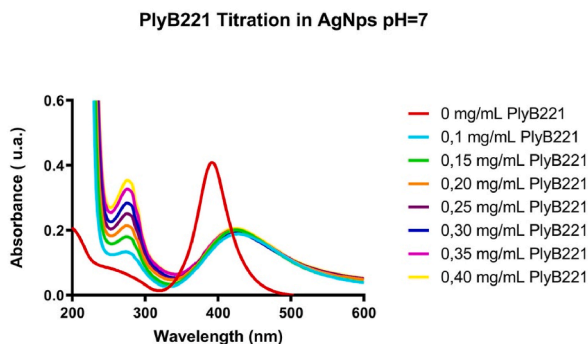

Fig. 4. UV–vis titration data of PlyB221 in 2.6. 10^{-4} mM AgNPs highlighting PlyB221 protein free (red) and yellow spectra after 0.4 mg/ml PlyB221. (For interpretation of the references to color in this figure legend, the reader is referred to the Web version of this article.)
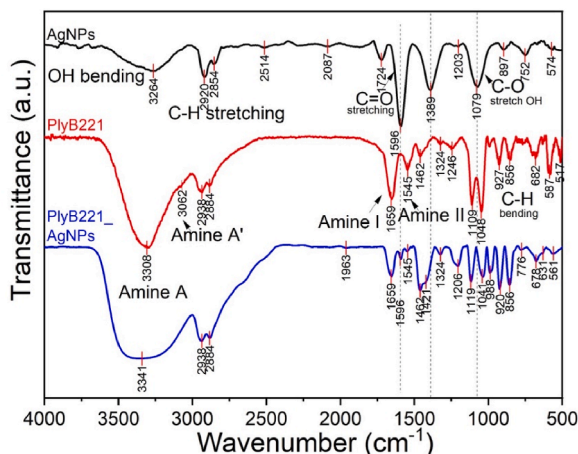

Fig. 5. FTIR spectra of synthesized AgNPs (black line), PlyB221 (red line) and AgNPs-PlyB221 complex (blue line). (For interpretation of the references to color in this figure legend, the reader is referred to the Web version of this article.)

at 1659 cm^{-1}, while the amine II band, which results from the combination of N–H in-plane bending and C–N stretching, is observed at 1545 cm^{-1}. Additionally, the amine III peak appears at 1324 cm^{-1} (Burt et al., 2004; Meutter and Goormaghtigh, 2021). The spectrum also exhibits vibrational active modes attributed to the side chains in the protein (Fig. 5). These include the C–H stretching mode at 2938 and 2884 cm^{-1} and the CH$_2$ bending mode at 1462 cm^{-1}, corresponding to potential residues of tyrosine protein. Other bands observed in the spectrum suggest the presence of cysteine sulfur (C–S stretching mode) and methionine at 682 cm^{-1} and 587 cm^{-1}, respectively (Burt et al., 2004; Leprince et al., 2020).

In the PlyB221-AgNPs complex, an overlap of the silver nanoparticles and protein bands was observed, which indicated that the bands associated with the polypeptide backbone were not cleaved during the conjugation process. Instead, a decrease in the intensity of bands associated with amine I and II, along with the characteristic band of AgNPs, was observed (Babu and Gunasekaran, 2009; Burt et al., 2004; Govindaraju et al., 2008). This decrease suggests a possible interaction between the C=O groups of both samples, possibly via hydrogen bonding, thereby stabilizing the nanoparticles in the protein matrix (Babu and Gunasekaran, 2009; Balaji et al., 2009; Burt et al., 2004). None significant shifts was observed in the bands from the functional groups of the protein, which play a crucial role in its bioactivity, with an increase in the intensity of the peak associated with the O–H bending band and CH$_2$ bending (Burt et al., 2004).

The size of the silver nanoparticle was found to be approximately 4 nm. The standard deviation, recorded as 0.70 ± 0.10 nm, indicates the remarkable uniformity and quality of the prepared dispersions. Zeta (ζ)-potential measurements play a crucial role in providing valuable data about nanoparticle agglomeration, distribution, and stability in solution (Edis et al., 2020). The AgNPs samples exhibited ζ-potential values close to −30 mV, indicating a high level of stability for the nanoparticles in the solution (Edis et al., 2020). Notably, the nanoparticles demonstrated exceptional stability over a period of approximately 30 days, as observed from consistent size, zeta potential, and Poly-Dispersity Index (PDI) values.

Prior to diluting the AgNPs, the hydrodynamic size distribution and zeta potential of PlyB221 were measured using DLS (Fig. 6). PlyB221 exhibited an average hydrodynamic size of 143.7 nm (St Dev 23.8 nm) and a zeta potential of −13.5 mV. The interaction between PlyB221 and AgNPs was investigated through Titration-DLS. The titration of PlyB221 into AgNPs resulted in an increase in the hydrodynamic diameter of AgNPs from 4 nm to a plateau of approximately 2000 nm, suggesting that the AgNPs were fully covered by proteins. The zeta potential changed from −30 mV to −15 mV, indicating possible formation of electrostatic interactions (see Table 1).

The morphology and structure of AgNPs were thoroughly investigated using SEM. The results revealed an average diameter of 10.74–15.25 nm for the AgNPs (Fig. 7). The nanoparticles exhibited a small size, indicative of an efficient synthesis process.

TEM has a high accuracy and reliability for determining the shape, distribution, size, and composition of NPs. The TEM images shown in Fig. 8(a) show that our sample is composed by well-dispersed spherical NPs. As highlighted in the HR-TEM image (inset) of a single NP, the measured distance of 2.36 Å between the crystallographic planes can be indexed to the (111) family of planes of Ag^0 with FCC structure (Machado et al., 2018), confirming the formation of Ag NPs. Furthermore, the EDS analysis of the sample (Fig. 8
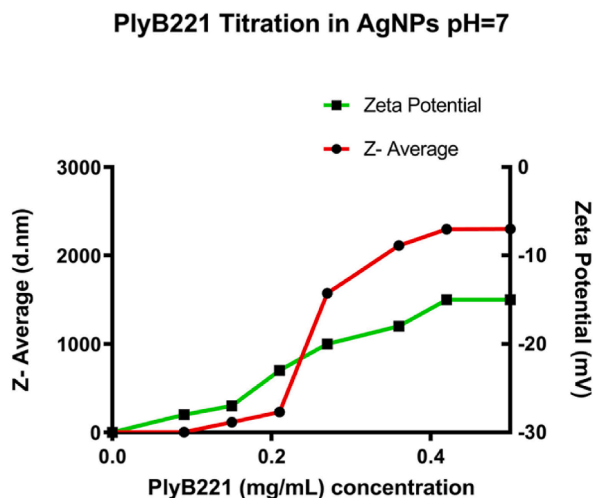

Fig. 6. Changes in the mean particle size (red) and ζ-potential (green) of AgNPs-PlyB221 complexes with increasing PlyB221 endolysin (the pH of PlyB221 endolysin and AgNPs are both at pH 6). (For interpretation of the references to color in this figure legend, the reader is referred to the Web version of this article.)

Table 1
Zeta potential measurements and DLS results for the AgNPs.

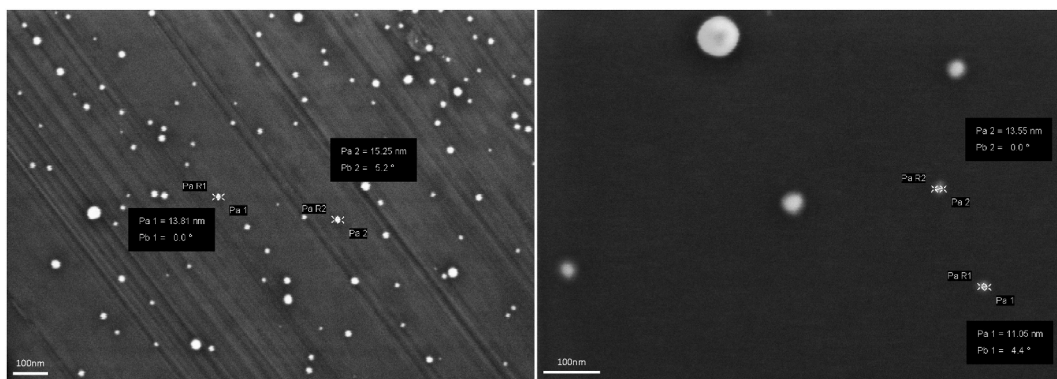| Sample	Zeta -Potential (mV)	Particle Size Mean (nm)	(PDI)
AgNPs (stability 1 day)	−34.4	3.77 ± 0.78	0.309
AgNPs (stability 30 days)	−37.8	3.27 ± 0.69	0.182

Fig. 7. SEM images of AgNPs obtained at 300× magnification with detail of nanoparticle size between 11 and 15 nm.
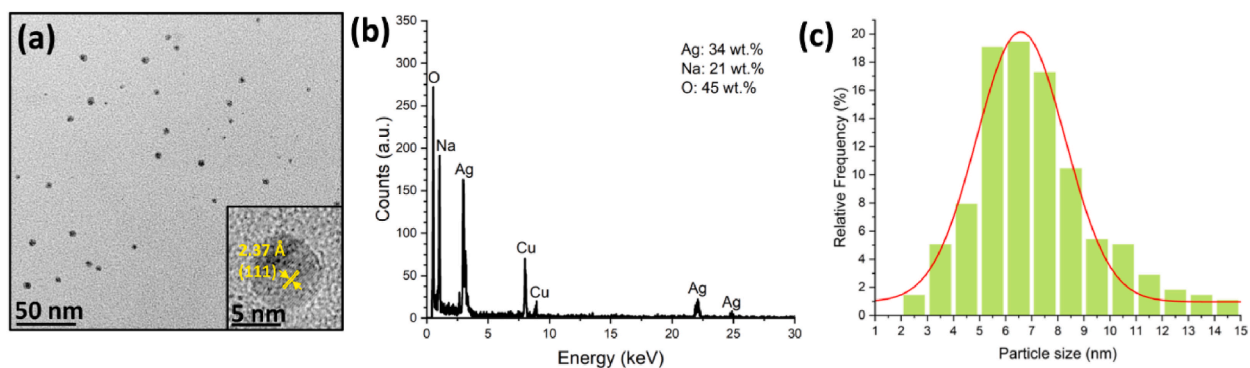

Fig. 8. (a) TEM image of Ag NPs and HRTEM image of a single NP (inset), (b) compositional analysis by EDS, and (c) estimation of Ag NPs size distribution.

(b)) revealed the presence of Ag, providing further evidence for the successful synthesis of AgNPs. The presence of Na and O elements primarily stems from the citrate functionalization using sodium citrate precursor, while the presence of Cu atoms is attributed to the TEM grid. The size of the NPs was estimated, and the results are shown in Fig. 8(c). The Ag NPs diameter fit well with a normal Gaussian distribution, giving an average value of 7.0 ± 3.5 nm closely related to the size results from DLS measurements. This result confirms the successful preparation of metallic Ag NPs.

Fig. 9(a–d) shows TEM images for AgNPs-PlyB221 complex. The bright field (BF) images in Fig. 9(a) and (b) reveal the presence of well-dispersed PlyB221 clusters with sizes ranging from 100 to 150 nm (Fig. 9(e)). This result matches well with those obtained via DLS characterization for PlyB221 and AgNPs-PlyB221 complex prepared at 100 µg.mL^{-1}. The dark field (DF) images shown in Fig. 9(c) and (d), generated by scattered electrons corresponding to (111) family of planes from Ag^0, evidence a homogeneous bright background with scattered bright spots, corresponding to PlyB221 and Ag NPs, respectively. This result suggests that the NPs are dispersed inside the PlyB221 clusters and proved the formation of protein corona in case of AgNPs-PlyB221 complex.

ITC was employed to gather information about the mode of interaction between the protein PlyB221 and the nanoparticle surface. It also allowed to measure the enthalpic and entropic contributions involved in the interaction of AgNPs with PlyB221.

Based on thermodynamic data, $\Delta H > 0$ and $\Delta S > 0$ correspond to hydrophobic forces, $\Delta H < 0$ and $\Delta S < 0$ correspond to van der Waals (vdW) forces and hydrogen bonding, and $\Delta H < 0$ and $\Delta S > 0$ correspond to electrostatic interactions (Rabbani et al., 2014).

Fig. 8 presents the original data isothermogram, showing the result of the titration of AgNPs with PlyB221, along with its derived parameters. The lower part of the plot (Fig. 10) displays the heat flow per mole of titrant (PlyB221) plotted against the molar ratio (AgNPs:PlyB221) for each injection, after subtracting the nanoparticle-buffer titration. The heat profile of the AgNPs and PlyB221 titration was fitted using a single-site binding model. The derived parameters indicate that the addition of the protein to the nanoparticles resulted in an exothermic binding reaction. The primary interactions governing the adsorption of PlyB221 onto AgNPs were identified as van der Waals and hydrogen bond interactions. This conclusion is based on the observation that the binding reaction was driven by an unfavorable change in entropy and a favorable change in enthalpy ($\Delta H = -2.59 \times 10^6 \pm 2.893 \times 10^5$ cal/mol, $\Delta S = -8.66$ kcal/mol/deg, and $\Delta G = -2.8$ kcal/mol). The negative value for the free energy suggests that the adsorption of PlyB221 onto the AgNPs interface is spontaneous, which is consistent with the findings of the surface potential neutralization study.

Assessing the potential interaction mechanisms between drugs and/or nanoparticles with proteins is one of the most intriguing analyses in ITC. It is known that interactions between nanoparticles and proteins are driven by non-covalent interactions, with electrostatic interactions, hydrophobic interactions, and hydrogen bonding commonly implicated in the protein-nanoparticle binding process (Cavalcanti et al., 2023).
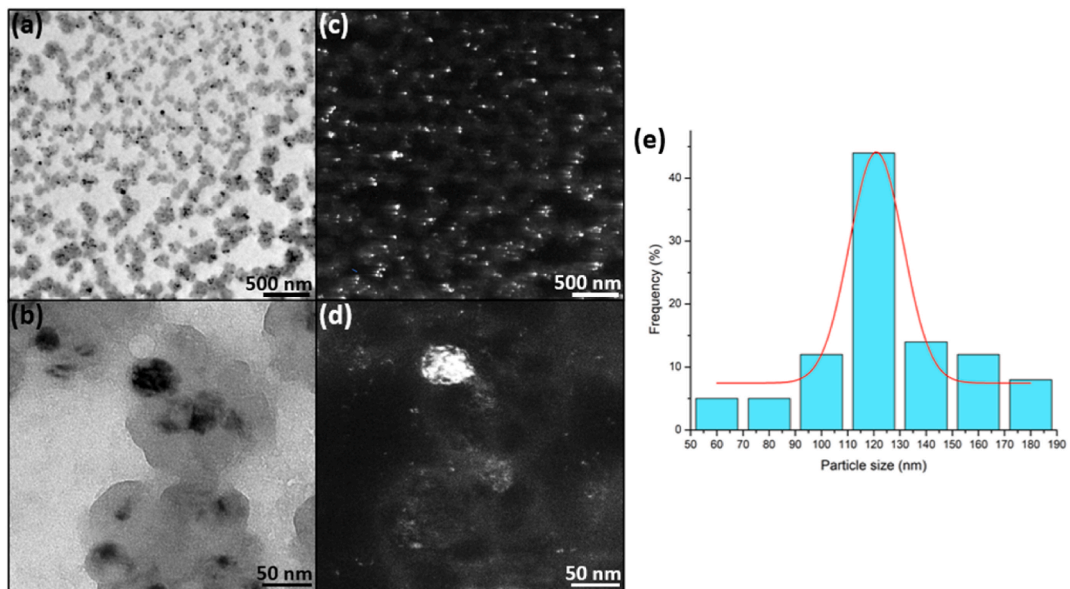
Fig. 9. TEM analysis of AgNPs-Ply221 complex prepared at 100 μg.mL-1. (a,b) BF images, (c,d) DF images, and (e) estimation of size distribution.
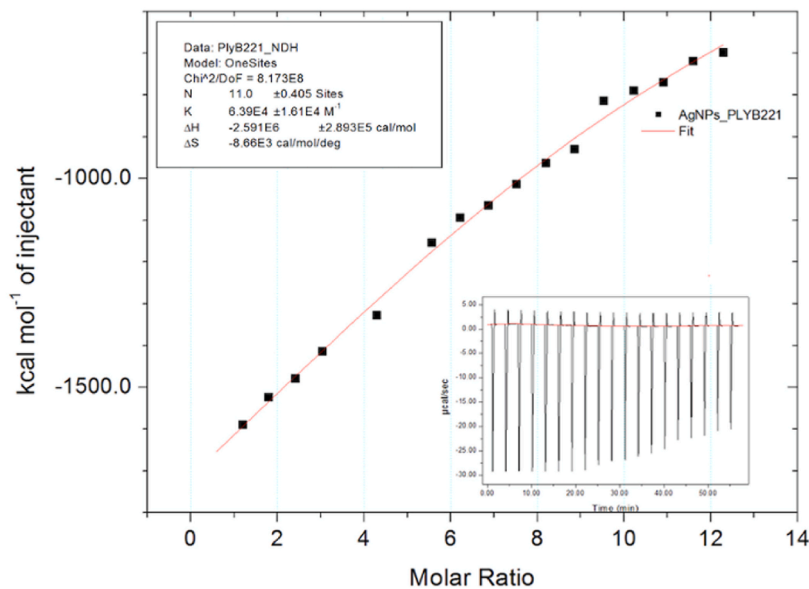

Fig. 10. ITC profiles of the interaction of PlyB221 with AgNPs.

The adsorption behavior of lactoferrin onto silver nanoparticles was investigated using the ITC technique in Nayak's and collaborators study (Nayak et al., 2019). The findings elucidate the involvement of van der Waals interactions and hydrogen bonding. Notably, there were no substantial impacts observed on the protein's conformation and stability. The study underscores that the creation of a corona around the silver nanoparticles enhances their cytotoxicity. In a separate study, Siddiq and colleagues (Siddiq et al., 2019) explored the impact of pH variations (4, 4.7, and 7.4) on the interaction between silver nanoparticles and bovine serum albumin using ITC. The outcomes indicated heightened interactions between albumin and silver nanoparticles at pH 7.4, exhibiting an enthalpy value (ΔH) of -2.1 ± 0.3 kJ mol-1. This process was characterized as exothermic and favored enthalpically, primarily driven by weak van der Waals/electrostatic interactions. Our results align with those previously reported, confirming the nature of the interaction between nanoparticles and proteins.

3.3. Antibacterial activity

The lytic activity of endolysin was evaluated in a turbidity reduction assay using *B. cereus*. Endolysins were sequentially diluted (from 0.253. 10^{-6} M to 8.125. 10^{-6} M) and incubated with bacteria resuspended in Tris-HCl buffer. The test was performed at 30 °C

and the OD was monitored for 30 min. Fig. 11 shows that at the highest concentration (i.e., 8.125. 10^{-6} M), PlyB221 induced a 70 % reduction in OD within 5 min of incubation.

Identical assays had been performed, assessing AgNPs, PlyB221 protein, and protein-nanoparticle complexes at defined concentrations, alongside control groups. Fig. 12 shows that the treatments were more effective in reducing turbidity than chlorophenicol. Furthermore, the association of AgNPs with PlyB221 was more effective than the others, promoting an 80 % reduction in turbidity.

Colorimetric activity assays were carried out to verify the metabolism of *B. cereus* after treatment with the samples. AgNPs, PlyB221 protein, and protein-nanoparticle complexes were serially diluted (from 0.126. 10^{-6} M to 4.06. 10^{-6} M) and incubated with bacteria in LB medium. In Fig. 13, it is evident that the combination of AgNPs with PlyB221 exhibited superior efficacy in diminishing the viability of *B. cereus* compared to other treatments, resulting in an impressive 60 % reduction in viability.

The inhibition percentage of *B. cereus* was computed employing the following equation (Allen et al., 2022), and the findings presented in Fig. 14 revealed a substantial 60 % inhibition when utilizing the combination of PlyB221 endolysin and AgNPs.

$$\left(1 - \frac{AMP\ sample - antibiotic\ control}{average\ treatment\ control - antibiotic\ control} \right) x\ 100$$

The lytic activity of Ag NPs with PlyB221 protein was also evaluated using negative-staining electron microscopy. Figs. 15 and 16 show STEM images obtained by SEM and TEM, respectively. The untreated control sample (Fig. 15(a and b) and 16(a,b)) reveals the natural morphology of *B. cereus* bacteria, with an intact cell wall structure displaying a normal aspect. Conversely, the treatment with Ag NPs and PlyB221 induces the lysis of the bacterial cell wall, as shown in Fig. 15(c and d) and 16(c,d) by the significant changes in bacterial morphology and integrity compared to the control sample.

The presence of *B. cereus* results in significant economic losses, impacting both the dairy industry due to the occurrence of thermophilic endospores and crop production as *B. cereus* is a psychrotrolant bacterium (Banerjee and Das, 2013). The combination of PlyB221 endolysin and silver nanoparticles (AgNPs) has proven effective in reducing this bacterium by 60 %. Our findings align with existing literature data regarding the use of phage-biocontrol (Cristobal-Cueto et al., 2021). This novel nanoconjugates can be applied as an additive in dairy industries and administered in irrigation water to mitigate losses caused by pathogenic bacteria in economically relevant crops, particularly when administered within a short period following infection (Cristobal-Cueto et al., 2021).
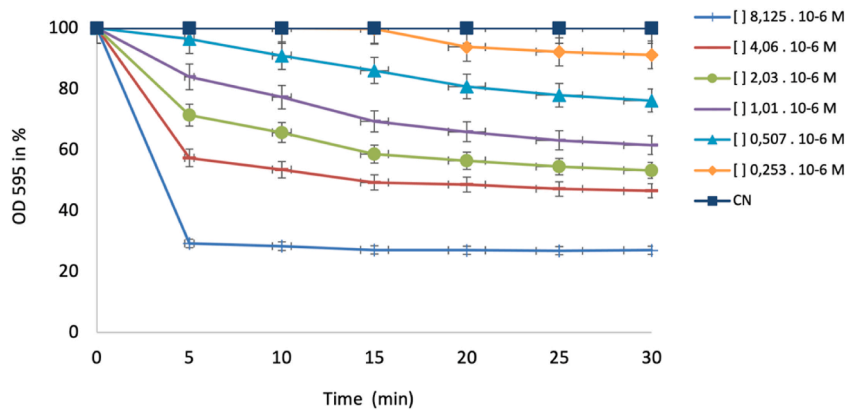

Fig. 11. Bacteriolytic activity of PlyB221 assessed by OD monitoring. The activity test was performed on exponentially growing *B. cereus* at 30 °C in the optimal buffer for endolysin and using enzyme concentrations ranging from 0.253. 10^{-6} M to 8.125. 10^{-6} M.
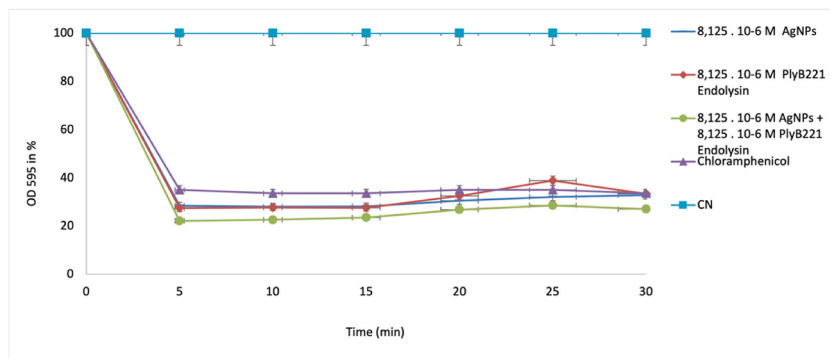

Figura 12. Bacteriolytic activity of AgNPs, PlyB221 protein, and protein-nanoparticle complexes at defined concentrations assessed by OD monitoring. The activity test was performed on exponential growth of *B. cereus* at 30 °C in the ideal buffer for endolysin and using fixed enzyme concentrations of 8125. 10^{-6} M.
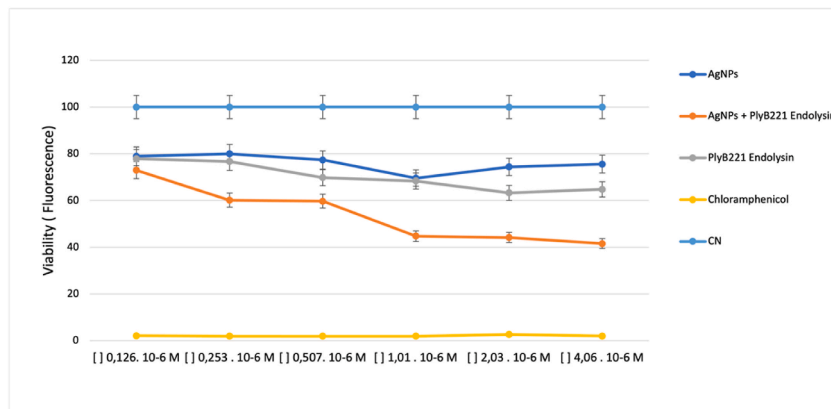
Fig. 13. Colorimetric assessment of AgNPs, PlyB221 protein, and protein-nanoparticle complexes via a series of treatment dilutions. The test involved incubation with 0.015 % resazurin for a duration of 4 h, with measurements taken using excitation at 530 nm and fluorescence emission recorded at 590 nm.
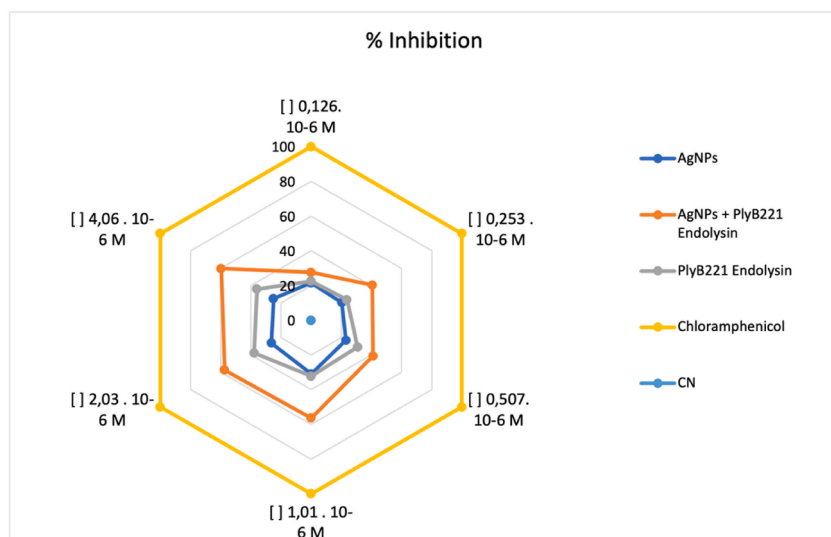

Fig. 14. Radar graph illustrating percentage inhibition of compounds against *B. cereus*. The yellow color corresponds to the highest inhibitions (more than 85 %). The orange zone represents 40–60 % inhibition, while the gray zone corresponds to 20–40 % inhibition. The experiment was conducted using chlorophenicol as standard. (For interpretation of the references to color in this figure legend, the reader is referred to the Web version of this article.)

Oh and colleagues (Oh et al., 2024) assessed the activity of endolysins LysPECP14 and LysPECP20 through a turbidity reduction assay in reference strains of *E. coli* O157:H7. They confirmed the considerable potential of these endolysins as highly versatile antimicrobials, applicable to thermal processes or critical phases involving multi-species bacterial contamination.

Others studies have focused on the use of endolysins as biocontrol agents to manage bacteria causing food poisoning. Successful utilization of certain endolysins has been documented in reducing foodborne bacteria (Chang et al., 2017; Love et al., 2018). For instance, in fresh milk, the C. perfringens endolysin LysCPAS15 (10.2 µg/mL) caused a 3-log reduction in 2 h (Cho et al., 2020). The endolysin cpp-lys (10 µg) reduced the viability of C. perfringens in lettuce by > 4 log CFU at 15 min, 30 min, and 60 min, respectively (Zhao et al., 2023). Listeria monocytogenes endolysins Ply500 (50 µg/mL) and LysZ5 (40 U ml-1) resulted in a 4-log reduction in romaine lettuce for 24 h and soy milk for 3 h, respectively (Bai et al., 2016). Furthermore, LysSTG2 (100 µg/mL), a novel endolysin from Salmonella phage STG2, reduced viable counts of Pseudomonas aeruginosa and Pseudomonas putida by 0.6 log in chicken samples and 1.1 log in salmon samples within 2 h (Zhang et al., 2022b). Many of these studies highlight the potential of endolysins in mitigating bacterial contamination in various food products.

The enzymatic activity of endolysin can be influenced by certain divalent metal ions, as indicated in various studies, while other metal ions may exert an inhibitory effect on endolysin activity (Zhao et al., 2023). The interaction of metal ions with specific amino acid residues in different domains of endolysins is suggested as a mechanism that modulates enzymatic activity, as highlighted in previous research (Fujiki et al., 2018; Son et al., 2012). Our results hold significant implications for the development of therapeutic platforms aimed at discerning and selectively eliminating super-resistant bacteria in agriculture using endolysin and silver nanoparticles. The data presented in this study underscores the viability of this application as a genuine choice in biocontrol.
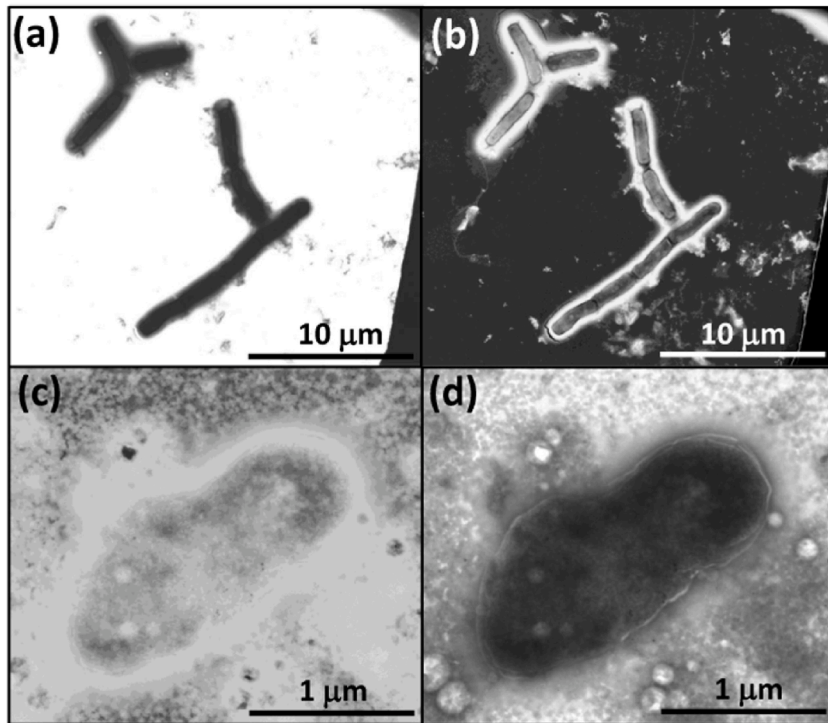
Fig. 15. STEM images obtained by negative-staining SEM characterization. (a) BF and (b) DF of *B. cereus* without treatment (control). (c) BF and (d) DF of *B. cereus* treated with protein-nanoparticle complexes.

4. Conclusion

An in-depth investigation of protein-corona formation on AgNPs and PlyB221 was conducted, revealing the spontaneous interaction of proteins on the surface of AgNPs. The binding process led to a reduction in the AgNPs' SPR band absorbance and a shift in the wavelength corresponding to the absorbance maximum from 396 nm to 420 nm. Additionally, there was a significant increase in the hydrodynamic diameter of AgNPs from 4 nm to a plateau of approximately 2000 nm, accompanied by a change in Zeta Potential (ZP) from −30mV to −15mV, indicating the complete coverage of AgNPs by proteins with electrostatic interactions. ITC analysis revealed a negative value for the free energy, a compelling indicator that PlyB221's adsorption onto the AgNPs interface occurred spontaneously. This corroborated the observations from the surface potential neutralization exploration. The binding reaction was propelled by an entropy alteration that skewed unfavorably and an enthalpy modification that leaned favorably. These parameters collectively underscore that the introduction of the protein to the nanoparticles kindled an exothermic binding reaction. These findings were further validated through FTIR and TEM analyses. The lytic activity results indicated that the combination of AgNPs with PlyB221 (at 8.125×10^{-6} M) successfully reduced the turbidity of *B. cereus* by 80 %. These results were further corroborated by the resazurin assay, where the inhibition percentage against *B. cereus* reached 60 % when using a concentration of 4.06×10^{-6} M. Our results hold significant implications for the development of biocontrol agents aimed at discerning and selectively eliminating super-resistant bacteria in agriculture.

Ethics approval and consent to participate

Not applicable.

Consent for publication

Not applicable.

Availability of data and materials

The datasets used and/or analyzed during the current study are available from the corresponding author on reasonable request.
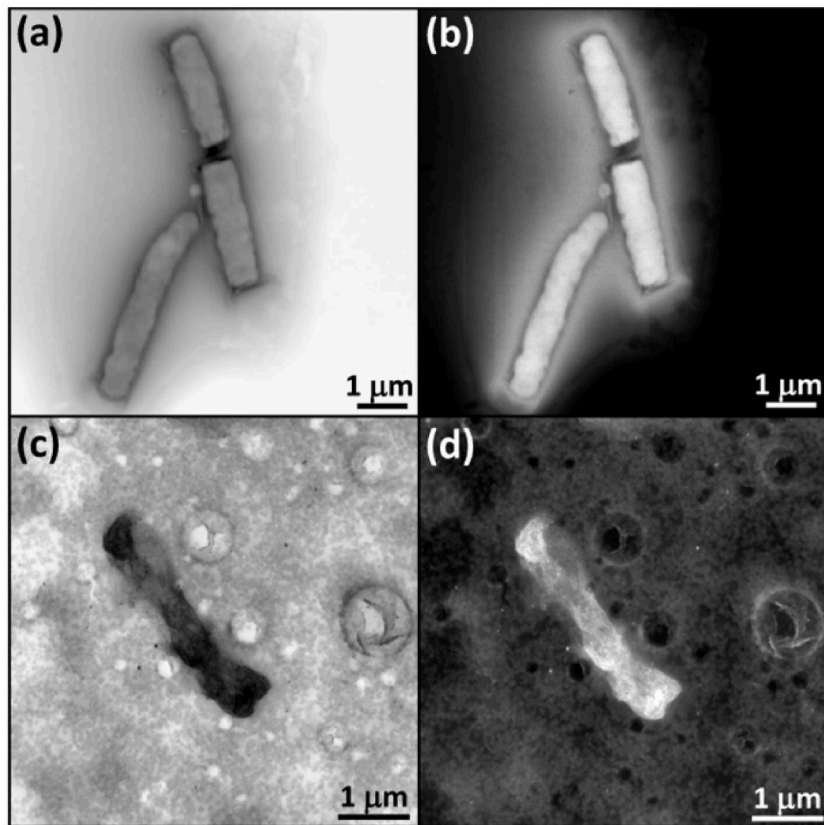
Fig. 16. STEM images obtained by negative-staining TEM characterization. (a) BF and (b) DF of *B. cereus* without treatment (control). (c) BF and (d) DF of *B. cereus* treated with protein-nanoparticle complexes.

CRediT authorship contribution statement

Fernanda Coelho: Writing – review & editing, Writing – original draft, Visualization, Validation, Project administration, Methodology, Investigation, Formal analysis. **Angelica Maria Mazuera Zapata:** Writing – original draft, Methodology, Investigation, Formal analysis. **Thales Rafael Machado:** Writing – original draft, Methodology, Formal analysis. **Fernanda Canduri:** Investigation. **Valtencir Zucolotto:** Writing – review & editing, Supervision, Project administration, Formal analysis.

Declaration of competing interest

The authors declare that they have no known competing financial interests or personal relationships that could have appeared to influence the work reported in this paper.

Fernanda Coelho reports financial support was provided by State of Sao Paulo Research Foundation. If there are other authors, they declare that they have no known competing financial interests or personal relationships that could have appeared to influence the work reported in this paper.

Data availability

No data was used for the research described in the article.

Abbreviations

AgNPs   Silver nanoparticles
DLS   Dynamic Light Scattering
FTIR   Fourier Transform Infrared Spectroscopy
ITC   Isothermal Titration Calorimetry
PDI   Poly-Dispersity Index

SEM   Scanning Electron Microscopy
SPR   Surface plasmon resonance
UV-VIS   UV–Visible spectrometry
TEM   Transmission Electron Microscopy

References

Allen, J.L., Kennedy, S.J., Shaw, L.N., 2022. Colorimetric assays for the rapid and high-throughput screening of antimicrobial peptide activity against diverse bacterial pathogens. Methods Enzymol. 663.

Aziz, S.B., Hussein, G., Brza, M.A., Mohammed, S.J., Abdulwahid, R.T., Saeed, S.R., et al., 2019. Fabrication of interconnected plasmonic spherical silver nanoparticles with enhanced localized surface plasmon resonance (Lspr) peaks using quince leaf extract solution. Nanomaterials 9 (11).

Babu, M.M., Gunasekaran, P., 2009. Production and structural characterization of crystalline silver nanoparticles from Bacillus cereus isolate. Colloids and Surfaces B: Biointerfaces. 74, 191–195.

Bai, J., Kim, Y.T., Ryu, S., Lee, J.H., 2016. Biocontrol and rapid detection of foodborne pathogens using bacteriophages and endolysins. Front. Microbiol. 7, 474.

Balaji, D.S., Basavaraja, S., Deshpande, R., Bedre, M.D., Prabhakar, B.K., Venkataraman, A., 2009. Extracellular biosynthesis of functionalized silver nanoparticles by strains of Cladosporium cladosporioides fungus. Colloids and Surfaces B: Biointerfaces. 68, 88–92.

Banerjee, V., Das, K., 2013. Interaction of silver nanoparticles with proteins, a characteristic protein concentration dependent profile of SPR signal. Colloids Surf., B 111, 71–79.

Bottone, E.J., 2010. Bacillus cereus, a volatile human pathogen. Clin. Microbiol. Rev. 23, 382–398.

Burt, J.L., Gutiérrez-Wing, C., Miki-Yoshida, M., José-Yacamán, M., 2004. Noble-metal nanoparticles Directly conjugated to Globular proteins. Langmuir 20, 11778–11783.

Cao, X., Han, Y., Li, F., Li, Z., McClements, D.J., He, L., Decker, E.A., Xing, B., Xiao, H., 2019. Impact of protein-nanoparticle interactions on gastrointestinal fate of ingested nanoparticles: not just simple protein corona effects. NanoImpact 13, 37–43.

Caruso, F., Hyeon, T., Rotello, V.M., 2012. Nanomedicine. Chem. Soc. 41, 2537–2538.

Cavalcanti, I.D.L., Junior, F.H.X., Magalhães, N.S.S., Nogueira, M.C.B.L., 2023. Isothermal titration calorimetry (ITC) as a promising tool in pharmaceutical nanotechnology. Int J Pharm 641.

Chang, Q., Wang, W., Regev- Yochay, G., Lipsitch, M., Hanage, W.P., 2014. Evol Appl 8 (3), 240–247.

Chang, Y., Kim, M., Ryu, S., 2017. Characterization of a novel endolysin LysSA11 and its utility as a potent biocontrol agent against Staphylococcus aureus on food and utensils. Food Microbiol. 68, 112–120.

Chang, Y., 2020. Bacteriophage-derived endolysins applied as potent biocontrol agents to enhance food safety. Microorganisms 5, 724.

Cho, J., Kwon, J., O'Sullivan, D., Ryu, S., Lee, J., 2020. Development of an endolysin enzyme and its cell wall-binding domain protein and their applications for biocontrol and rapid detection of Clostridium perfringens in food. Food Chem. 345, 128562.

Ciepluch, K., Skrzyniarz, K., Barrios-Gumiel, A., Quintana, S., Sanchez-Nieves, J., Mata, F.J., Maciejewska, B., et al., 2019. Dendronized silver nanoparticles as bacterial membrane Permeabilizers and their interactions with P. aeruginosa Lipopolysaccharides, Lysozymes, and phage-derived endolysins. Front. Microbiol. 10, 2771.

Ciobanu, V., Roncari, F., Ceccone, G., Braniste, T., Ponti, J., Bogni, A., et al., 2022. Protein-corona formation on aluminum doped zinc oxide and gallium nitride nanoparticles. J. Appl. Biomater. Funct. Mater. 20.

Cristobal-Cueto, P., Garcia-Quintanilla, A., Esteban, J., Garcia- Quintanilla, M., 2021. Phages in food industry biocontrol and Bioremediation. Antibiotics 10, 786.

Dara, P.K., Mahadevan, R., Digita, P.A., Visnuvinayagam, S., Kumar, L.R.G., Mathew, S., et al., 2020. Synthesis and biochemical characterization of silver nanoparticles grafted chitosan (Chi-Ag-NPs): in vitro studies on antioxidant and antibacterial applications. SN Appl. Sci. 2 (4).

Dawson, K.A., Yan, Y., 2021. Current understanding of biological identity at the nanoscale and future prospects. Nat Nanotechonol 16, 229–241.

Edis, Z., Bloukh, S.H., Ibrahim, M.R., Sara, H.A., 2020. "Smart" antimicrobial Nanocomplexes with potential to decrease Surgical site infections (SSI). Pharmaceutics 12 (4).

Fujiki, J., Nakamura, T., Furusawa, T., Ohno, H., Takahashi, H., Kitana, J., Usui, M., Higuchi, H., Tanji, Y., Tamura, Y., Iwano, H., 2018. Characterization of the lytic capability of a LysK-like endolysin, Lys-phiSA012, derived from a polyvalent Staphylococcus aureus bacteriophage. Pharmaceuticals 11, 25.

Ghosh, G., Panicker, L., 2021. Protein–nanoparticle interactions and a new insight. Soft Matter 17, 3855–3875.

Govindaraju, K., Basha, S.K., Kumar, V.G., Singaravelu, G., 2008. Silver, gold and bimetallic nanoparticles production using single-cell protein (Spirulina platensis) Geitler. J. Mater. Sci. 43 (15), 5115–5122.

Hajipour, M.J., Fromm, K.M., Ashkarran, A.A., et al., 2012. Antibacterial properties of nanoparticles. Trends Biotechnol. 30, 499–511.

Hu, X.Y., Logue, M., Robinson, N., 2020. Antimicrobial resistance is a global problem – a UK perspective. European Journal of Integrative Medicine 36, 101136.

Ismail, M., Gul, S., Khan, M.I., Khan, M.A., Asiri, A.M., Khan, S.B., 2019. Medicago polymorpha-mediated antibacterial silver nanoparticles in the reduction of methyl orange. Green Process. Synth. 8 (1), 118–127.

Jana, N.R., Gearheart, L., Murphy, C.J., 2001. Seeding growth for size control of 5-40nm diameter gold nanoparticles. Lagmuir 17 (22), 6782–6786.

Kong, M., Na, H., Ha, N.C., Ryu, S., 2019. LysPBC2, a novel endolysin Harboring a Bacillus cereus spore binding domain. Appl. Environ. Microbiol. 85, e02462-18.

Kulshrestha, S., Khan, A.U., 2018. Nanomedicine for anticâncer and antimicrobial treatmente: an overview. IET Nanobiotechnol. 12, 1009–1017.

Lara, H.H., Ayala-Nunez, N.V., Tuurent, L.D.C.I., et al., 2010. Bactericidal effect of silver nanoparticles against multidrug-resistant bactéria. World J. Microbiol. Biotechnol. 26, 6715–6721.

Leprince, A., Nuytten, M., Gillis, A., Mahillon, J., 2020. Characterization of PlyB221 and PlyP32, two novel endolysins encoded by phages preying on the Bacillus cereus Group. Viruses 12 (9).

Love, M., Bhandari, D., Dobson, R., Billington, C., 2018. Potential for bacteriophage endolysins to supplement or replace antibiotics in food production and clinical care. Antibiotics 7, 17.

Machado, T., Macedo, N., Assis, et al., 2018. From complex Inorganic Oxides to Ag-Bi Nanoalloy: synthesis by Femtosecond laser Irradiation. ACS Omega 3, 9880–9887.

Mann, A., Nehra, K., Twinkle, J.S.R., 2021. Antibiotic resistance in agriculture: Perspectives on upcoming strategies to overcome upsurge in resistance. Curr Res Microb Sci 2, 100030.

Melo, M.A., Santos, L.S.S., Gonçalves, M.C., Nogueira, A.F., 2012. Preparação de nanopartículas de prata e ouro: um método simples para a introdução da nanociência em laboratório de ensino. Quim. Nova 35.

Meutter, J., Goormaghtigh, E., 2021. Evaluation of protein secondary structure from FTIR spectra improved after partial deuteration. Eur. Biophys. J. 50 (3–4), 613–628.

Miller, M.A., Gadde, S., Pfirschke, C., Engblom, C., Sprachman, M.M., Kohler, R.H., et al., 2015. *Sci Transl Med.* Predicting Therapeutic Nanomedicine Efficacy Using a Companion Magnetic Resonance Imaging Nanoparticle, vol. 5.

Muzamil, M., Khalid, N., Aziz, M.D., Abbas, S.A., 2014. Synthesis of silver nanoparticles by silver salt reduction and its characterization. EIOP Conference Series: *Materials Science and Engineering.* Institute of Physics Publishing.

Nayak, P.S., Borah, S.M., Gogoi, H., Asthana, S., et al., 2019. Lactoferrin adsorption onto silver nanoparticle interface: implications of corona on protein conformation, nanoparticle cytotoxicity and the formulation adjuvanticity. Chen. Eng. J. 361, 470–484.

Oh, M., Cevallos-Urena, A., Kim, B.S., 2024. Bacteriophages PECP14, PECP20, and their endolysins as effective biocontrol thers for Escherichia coli O157:H7 and ther foodborne pathogens. Int J Microbol.

Paino, I.M.M., Zucolotto, V., 2015. Poly(vinyl alcohol)-coated silver nanoparticles: Activation of neutrophils and nanotoxicology effects in human hepatocarcinoma and mononuclear cells. Environ. Toxicol. Pharmacol. 39 (2), 614–621.

Park, K.M., Kim, H.J., Jeong, M., Koo, M., 2020. Enterotoxin genes, antibiotic Susceptibility, and biofilm formation of low-temperature-Tolerant Bacillus cereus isolated from green leaf lettuce in the Cold chain. Foods 25 (3), 249.

Pastorizo-Santos, I., Liz-Marzán, L.M.N., 2009. N-dimethylformamide as a reaction medium for metal nanoparticle synthesis. Adv. Funct. Mater. 19 (5), 679–688.

Rabbani, G., Khan, M.J., Ahmad, A., Maskat, M.Y., Khan, R.H., 2014. Effect of copper oxide nanoparticles on the conformation and activity of β-galactosidase. Colloids Surf B *Biointerfaces*. 123, 96–105.

Siddiq, A.M., Murugan, D., Srivastava, R., Alam, M.S., 2019. Influence of pH on interaction of silver nanoparticles-protein: analyses by spectroscopic and thermodynamic ideology. Colloids Surf. B Biointerfaces 184, 1–11.

Siriwardana, K., Wang, A., Gadogbe, M., Collier, W.E., Fitzkee, N.C., Zhang, D., 2015. Studying the effects of cysteine residues on protein interactions with silver nanoparticles. J. Phys. Chem. C 119 (5), 2910–2916.

Solomon, S., Bahadori, M., Jeyarajasingam, A.V., Rutkowsky, S.A., Boritz, C., Mulfinger, L., 2007. Synthesis and Study of Silver Nanoparticles.

Son, B., Yun, J., Lim, J., Shin, H., Heu, S., Ryu, S., 2012. Characterization of LysB4, an endolysin from the Bacillus cereus-infecting bacteriophage B4. BMC Microbiol. 12, 33.

Tolba, M., Ahmed, M.U., Tlili, C., Eichenseher, F., Loessner, M.J., Zourob, M., 2012. A bacteriophage endolysin-based electrochemical impedance biosensor for the rapid detection of Listeria cells. Analyst 137, 5749.

Zhang, Y., Huang, H., Duc, H., Masuda, Y., Honjoh, K., Miyamoto, T., 2022. Application of endolysin LysSTG2 as a potential biocontrol agent against planktonic and biofilm cells of Pseudomonas on various food and food contact surfaces. Food Control 131, 108460.

Zhao, X., Li, L., Zhang, Q., Li, M., et al., 2023. Characterization of the Clostridium perfringens phage endolysin cpp-lys and its application on lettuce. Int J Foof Microbiol.